Magnetic Domain States and Critical Sizes in the Titanomagnetite Series

Brendan Cych[1], Greig A. Paterson[1], Lesleis Nagy[1], Wyn Williams[2], Bruce Moskowitz[3]

[1]Department of Earth, Ocean and Environmental Sciences, University of Liverpool, Liverpool, L69 7ZE, UK
[2]School of GeoSciences, University of Edinburgh, Grant Institute, West Mains Road, Edinburgh, EH9 3JW, UK
[3]Institute for Rock Magnetism, Department of Earth and Environmental Sciences, University of Minnesota, 150 John T. Tate Hall, 116 Church St. SE, Minneapolis, MN 55455U, USA

Key Points:

- We systematically map out the domain states in titanomagnetite as a function of shape and composition.
- Our results highlight ranges of compositions, shapes and sizes which contain unreliable paleomagnetic recorders.
- For certain shapes and compositions, these regions span hundreds of nanometers, representing a significant proportion of remanence carriers.

Abstract

The minerals carrying the magnetic remanence in geological samples are commonly a solid solution series of iron-titanium spinels known as titanomagnetites. Despite the range of possible compositions within this series, micromagnetic studies that characterize the magnetic domain structures present in these minerals have typically focused on magnetite. No studies systematically comparing the domain-states present in titanomagnetites have been undertaken since the discovery of the single vortex (SV) structure and the advent of modern micromagnetism. The magnetic properties of the titanomagnetite series are known to vary strongly with composition, which may influence the domain states present in these minerals, and therefore the magnetic stability of the samples bearing them.

We present results from micromagnetic simulations of titanomagnetite ellipsoids of varying shape and composition to find the size ranges of the single domain (SD) and SV structures. These size ranges overlap, allowing for regions where the SD and SV structures are both available. These regions are of interest as they may lead to magnetic instability and "pTRM tails" in paleointensity experiments. We find that although this SD+SV zone occupies a narrow range of sizes for equidimensional magnetite, it is widest for intermediate (TM30-40) titanomagnetite compositions, and increases for both oblate and prolate particles, with some compositions and sizes having an SD+SV zone up to 100s of nm wide. Our results help to explain the prevalence of pTRM tail-like behavior in paleointensity experiments. They also highlight regions of particles with unusual domain states to target for further investigation into the definitive mechanism behind paleointensity failure.

Plain Language Summary

Rocks that record Earth's magnetic field often contain the mineral magnetite. The crystal structure of magnetite allows titanium atoms to substitute for iron, giving rise to a range of minerals known as titanomagnetites. The internal magnetic structure of titanomagnetite particles in rocks, known as the "domain structure", controls the ability of that particle to record magnetic fields. Particles with certain kinds of domain structure are unstable magnetic recorders, which can cause problems for experiments trying to determine Earth's magnetic field strength in the past (paleointensity experiments). Although the domain structures in magnetite are well understood, there are no recent studies which describe them in titanomagnetites.

In this paper, we simulate the domain structures in small titanomagnetite particles and map these out as a function of size, shape and chemical composition. In doing so, we identify types of magnetic particles with multiple possible domain structures that may give rise to unstable magnetizations. Our results indicate that some titanomagnetite particles may have unstable magnetizations over a much larger range of sizes than has previously been seen in magnetite. This wide range of sizes could explain the high failure rates of paleointensity experiments.

1 Introduction

Magnetite is one of the most important magnetic minerals in igneous and sedimentary rocks, commonly forming during the crystallization of basaltic magmas, and in sediments through erosional and biogenic processes. Stoichiometrically pure magnetite (Fe_3O_4) is a well studied magnetic mineral, but in nature it forms a solid solution series with titanium rich ulvospinel (Fe_2TiO_4). Titanomagnetite compositions within the series $Fe_{3-x}Ti_xO_4$ ($0 \leq x \leq 1$) are represented using the notation TMx (e.g. $x = 0.6$ is TM60). Fundamental magnetic properties of the titanomagnetites, including the Curie temperature (Nishitani & Kono, 1983), saturation magnetization (Bleil, 1976) and magnetocrystalline anisotropy constants (Kąkol et al., 1994), have been observed to vary across the solid solution se-

ries. The distribution of Curie temperatures in igneous rocks compiled from a compilation of 38 papers indicate that approximately 75% of paleomagnetic samples do not contain pure magnetite (see supplementary information for detailed references). Instead, they suggest that compositions from TM0 to TM60 are prevalent along with other minerals. Despite this wide range of compositions and behaviours in nature, the rock magnetic properties of titanomagnetites and their influences on paleomagnetic experiments are understudied.

Rocks containing titanomagnetites are used to determine Earth's magnetic field strength and direction in the distant past. This information has many practical applications in the geosciences, from detecting the age of archeological samples, to determining the motion of tectonic plates and the nucleation age of Earth's inner core. The fundamental physics that explain how a rock can record a thermal remanent magnetization (TRM) by cooling in a field was first described by Louis Néel (Néel, 1949). This work assumes that the magnetic particles contained within rocks are uniformly magnetized in a structure known as "single-domain" (hereafter referred to as SD). Unfortunately, the SD structure is only energetically efficient over a small range of particle sizes, and the majority of the magnetization in natural materials is carried by particles in other states, as we show below. Consequently, paleomagnetic experiments often produce results that are complicated and difficult to interpret. A better understanding of the domain states present in magnetic materials is necessary to understand this behavior, and to ensure that paleomagnetists can obtain accurate results.

To determine the dominant domain states of a magnetic particle, researchers use the micromagnetic modelling approach of Brown (1963). This technique was adapted by Fredkin and Koehler (1987) into a computational finite-element based technique, which finds stable magnetization states that minimize the energy of the particle. Some of the earliest findings from this approach demonstrated that magnetite particles sized approximately 100 nm - 1 μm have magnetizations which curl in a "vortex" shape around a uniform core, known as the Single Vortex (SV) structure (Schabes & Bertram, 1988; W. Williams & Dunlop, 1989).

Recent work has shown that there is an "unstable zone" (where particle relaxation times drop precipitously) in equidimensional magnetite particles at the lower size limit of the SV structure. In this region, the dominant domain state is a single vortex with the vortex core aligned along a magnetocrystalline hard axis direction . The energy needed to escape this state is small, and so it is not stable over geological timescales. Nagy et al. (2022) additionally showed that competition between shape easy- and hard-aligned SV states in magnetite can produce complicated "partial TRM (pTRM) tail" behaviour similar to that frequently seen in paleointensity experiments (e.g. Bol'Shakov, 1979; Dunlop & Özdemir, 2001; Riisager & Riisager, 2001; Santos & Tauxe, 2019).

Several studies have focused on determining the range of sizes and shapes over which domain states are stable in metallic iron (Muxworthy & Williams, 2015), magnetite (Muxworthy & Williams, 2006; Nagy et al., 2019), and greigite (Muxworthy et al., 2013; Valdez-Grijalva et al., 2018). Despite the range of titanomagnetite compositions prevalent in nature, there has been little work published on domain states in titanomagnetites since Butler and Banerjee (1975). That study showed that the size range over which the SD structure was stable varied as a function of TM composition. Moskowitz (1980) and Moskowitz and Halgedahl (1987) followed this work, calculating this size range for TM60 as a function of oxidation, temperature and stress. These two studies were undertaken before the discovery of the SV structure, instead considering a transition between a single domain and the two-domain structure of Kittel (1949). Muxworthy and Williams (2006) used micromagnetic modelling to determine the range of sizes for which the SD and SV structures were available in elongated magnetite cuboids. This range of sizes differed significantly from that of Butler and Banerjee (1975), but a modern micromagnetic approach was not applied to other TM compositions. Khakhalova et al. (2018) simulated single and multi-

vortex states in a large pyramidal TM54 particle, but did not explore the variation in domain state with the size and shape of particles.

In this paper, we present results from a series of micromagnetic models using the Micromagnetic Earth Related Robust Interpreted Language Laboratory (MERRILL; Ó Conbhuí et al., 2018) software package, v1.8.6p. Each simulation determines the range of possible sizes over which the single domain and single vortex structures can exist using a "size hysteresis" algorithm (e.g. Witt et al., 2005; Muxworthy & Williams, 2006, 2015; Nagy et al., 2019) where a minimum energy state is calculated in a titanomagnetite particle whilst progressively varying its size (described fully in Section 2.1). We perform these simulations for ellipsoidal titanomagnetite particles of varying composition and axial ratio, from oblate to prolate. Our results, which are presented in Section 3 give the size ranges for the SD and SV structures for a range of TM compositions and prolate and oblate particles. This expands on the existing results of Muxworthy and Williams (2006) for prolate magnetites by more than an order of magnitude. We discuss the implications of these results, as well as the potential impact on paleomagnetic experiments in Section 4.

2 Methodology

2.1 The size hysteresis algorithm

For each geometry and titanomagnetite composition in this paper, we use a "size hysteresis" algorithm. A graphical example for a sphere of TM25 is shown in Figure 1. The algorithm works as follows:

1. For a 40 nm particle of a particular titanomagnetite composition and geometry, start with a uniform magnetization aligned along one of the magnetocrystalline easy axes in zero external field. An energy minimization is performed using MERRILL on this particle, producing a magnetization that is a local energy minimum (LEM) state.
2. The magnetization is taken and scaled up to a particle of a slightly larger size. An energy minimization is then performed on the new particle size. We define our size using the diameter of a sphere with equivalent volume (referred to as ESVD; equivalent spherical volume diameter). We increase the particle size by 10 nm when the ESVD is between 40 and 250 nm, and steps of 25 nm are used from 250 to 500 nm.
3. For a certain size range, the particle will remain in the SD structure (Figure 1 i.), but at some critical size, the SD structure stops being energetically favorable, and the domain state collapses to the SV structure (Figure 1 ii.). We call the diameter associated this size $d_{\max}$, which is defined as being the center point between the SD and SV structures (e.g. between Figure 1 i. and ii.).
4. We continue this process of scaling the magnetization onto particles of progressively larger sizes and minimizing the energy, repeating up to a size of 500 nm.
5. After reaching 500 nm, we reverse the process, mapping the magnetization onto progressively smaller particles and minimizing the energy. At some point, (between Figure 1 iii. and iv.), the particle transitions from the SV structure to the SD structure. We call this size $d_{\min}$, which may differ from $d_{\max}$.

As can be seen from Figure 1, the critical sizes for transitioning between the SD and SV structures and vice-versa are not the same, with $d_{\max}$ occurring at a larger size (165 nm) than $d_{\min}$ (105 nm). During the "shrinking" branch of the magnetization, we observe a hard-aligned vortex (Figure 1 iii.). The region between $d_{\min}$ and $d_{\max}$ is therefore of interest as it may contain the "unstable zone" of Nagy et al. (2017).

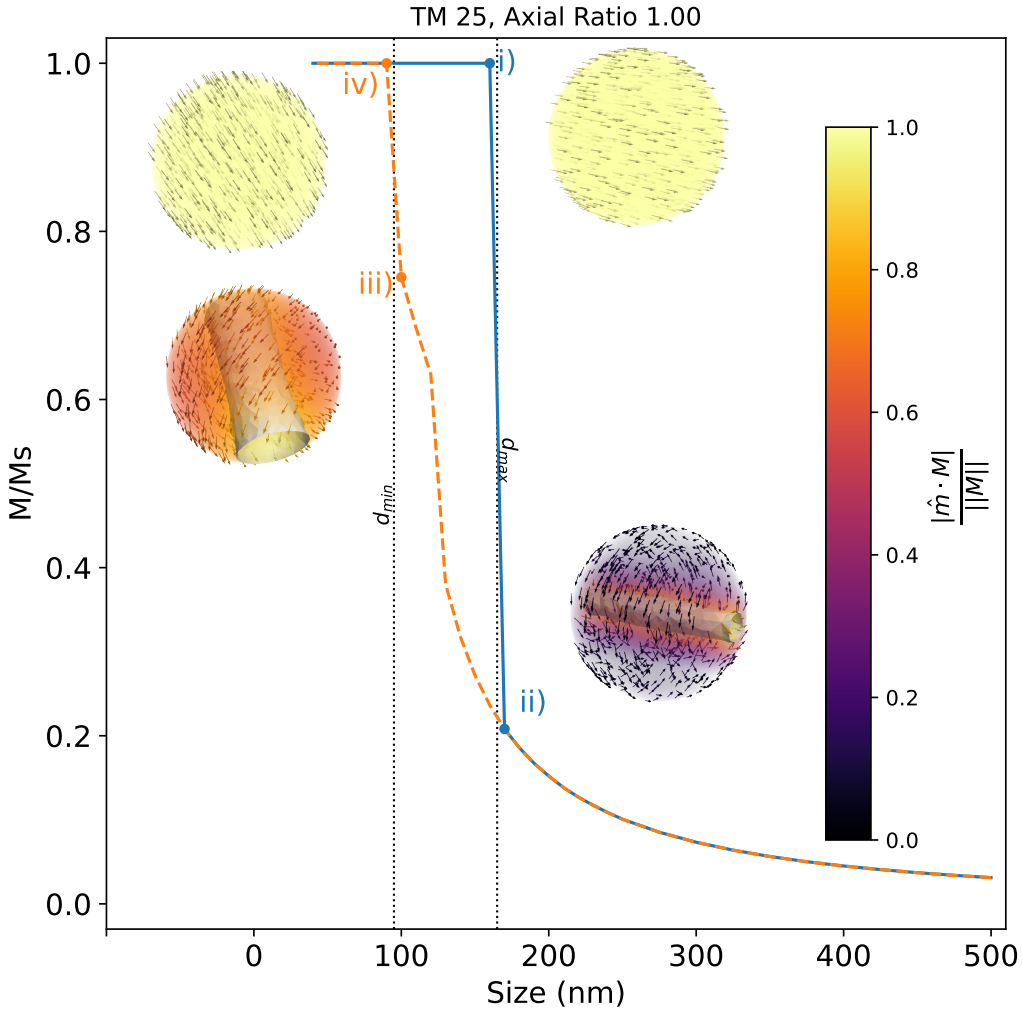

Figure 1. Ratio of the magnetization over the saturation magnetization (M/M_s) plotted against EVSD (nm) in a "size hysteresis loop" for a sphere of TM25. The blue solid line represents the magnetization as the particle is grown from 40 from 500 nm, and the orange dashed line represents the magnetization as it is shrunk from 500 nm to 40 nm. Example magnetization states from the loop are shown at points i - iv). Vectors represent the direction of the magnetization at that location in the particle. Grey cylinder in ii) and iii) represents an isosurface where the relative helicity (h_{rel}, described in the supplemental information) is 0.95. Colors represent the absolute value of the dot product of these vectors with the direction of the net magnetization, with lighter yellow regions being aligned with the net magnetization, and darker purple regions being perpendicular. The magnetization transitions from the SD to the vortex state between i) and ii) (160-170 nm) and the magnitude of the magnetization continues to be reduced up to 500 nm due to the tightening of the vortex core. The vortex rotates to a magnetocrystalline hard axis direction between ii) and iii) and transitions back into a single domain state between iii) and iv) (100-90 nm) along a different easy direction. $d_{\min}$ and $d_{\max}$ are plotted as vertical lines.

2.2 Compositions and geometries

In this study, we will test the effects of titanomagnetite composition as well as shape on d_{max} and d_{min}. To produce a micromagnetic model using a particular material, fundamental material parameters are needed: the Curie temperature T_{c}, saturation magnetization M_{s}, exchange constant A_{ex} and magnetocrystalline anisotropy constants k_1 and k_2. An extensive set of experimental data from previous work was compiled. Polynomial fits to these data were used to obtain functions that can return the material parameters for a given TM composition. Details of the datasets and resulting parameters used in this study are given in the Supplemental Material.

We applied the size hysteresis algorithm to ellipsoids of rotation with thirteen different axial ratios, logarithmically spaced between 1/3 and 3. A set of thirteen different titanomagnetite compositions was used, in 5% increments from 0% to 60% Ti. Tetrahedral meshes were produced for each size, shape and composition using the Coreform Cubit software package (Coreform LLC, 2017). The coarseness of the mesh used depended on the size of the geometry (keeping minimum number of elements to $\sim$ 15000) and the exchange length (λ_{ex}; Rave et al., 1998) of the material. For some combinations of composition and geometry, d_{max} was not reached by a size of 500 nm. In these cases, we ran the algorithm to a size of 1 μm (in steps of 50 nm to 800 nm, then 100 nm to 1 μm), with a set of meshes using a maximum of a million elements. This meant that some meshes exceeded $_{\mathrm{ex}}$ and so d_{max} values greater than 500 nm should be considered less precise. If d_{max} was greater than 1 μm, then it was not reported, and d_{min} was instead obtained by forcing a vortex state initial condition at 500 nm and proceeding with the "shrinking" branch as normal.

For each composition and geometry, two size hysteresis simulations were run, one in which the major axis of the ellipsoid was aligned with the magnetocrystalline easy axis of the material (referred to as "magnetocrystalline easy-shape easy" or ME-SE), and one in which it was aligned with the magnetocrystalline hard axis (referred to as "magnetocrystalline hard-shape easy" or MH-SE). The results displayed in Section 3 were produced by taking the maximum d_{max} and minimum d_{min} of the two datasets for each composition and geometry, and the resulting surfaces were interpolated by a 2d cubic spline using the SciPy package (Virtanen et al., 2020). The difference between results from the ME-SE and MH-SE datasets are discussed in Sections 3.2 and 3.3.

The LEMs at each step in the size hysteresis loop were visualized using the ParaView software (Ayachit, 2015). For each visualization, the relative helicity h_{rel} was calculated (see supplementary material for details). To determine d_{min} and d_{max}, the SV structure was identified by the presence of a coherent cylindrical isosurface at h_{rel}=0.95 containing a "vortex core" intersecting the surface of the particle in two places, and the SD structure was identified by the absence of such a core. Examples of SV structures with vortex cores can be seen in Figure 1 ii and iii). When visualizing LEM states, the volume and magnetization arrows are colored by the absolute cosine of the angle between the individual magnetization vectors and the particle's net magnetization. The lighter colours in the cores of vortex structures demonstrate that the bulk of the magnetization is carried in this core, and that the volume of the core influences the magnitude of the net magnetization.

3 Results

3.1 Anisotropy energies of the titanomagnetite series

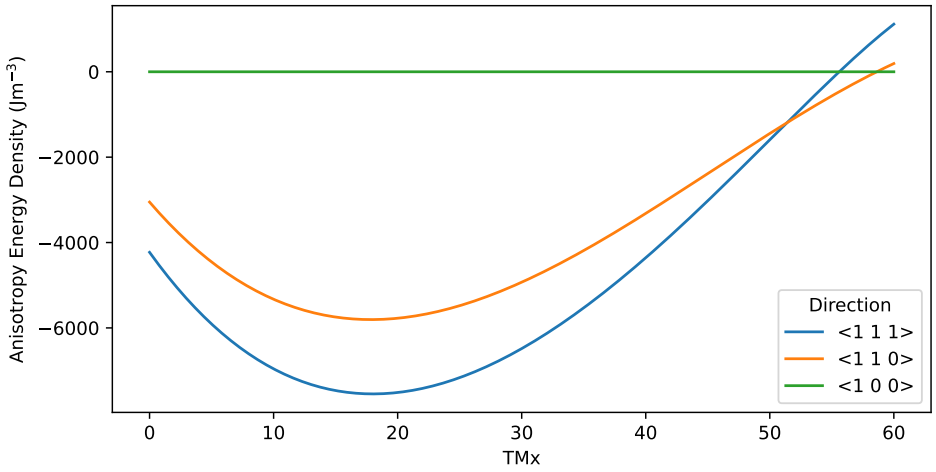

Figure 2. Magnetocrystalline anisotropy energy densities for an SD titanomagnetite particle as a function of composition. Different coloured lines are the anisotropy energy density for different magnetocrystalline directions. The line with the lowest (most negative) magnetocrystalline energy density is the easy axis.

Figure 2 shows the magnetocrystalline energy densities in SD titanomagnetites for the <1 0 0>, <1 1 0> and <1 1 1> directions obtained from our fit to experimental data for the k_1 and k_2 anisotropy constants. The magnetocrystalline easy axis for a particle can be determined by the lowest (most negative) energy. Anisotropy properties change significantly across the titanomagnetite series, the easy axis is along <1 1 1> for TM0 - 50, changing to <1 1 0> at $\sim$ TM51 and <1 0 0> at $\sim$ TM59. The hard axis is <1 0 0> from TM0 - 55 and changes to <1 1 1> just above TM55. The difference in anisotropy energy between the easy and hard directions reaches a maximum at $\sim$ TM20, and is significantly smaller at high TM compositions ($\geq$TM40).

3.2 Observed states

Examples of typical states observed during the size hysteresis algorithm are shown in Figures 1 and 3. Spherical particles behaved as in Figure 1, with the SD structure changing into an SV structure on the growing branch and back to an SD structure on the shrinking branch, usually rotating to a magnetocrystalline hard direction close to $d_{\min}$ on the shrinking branch (Figure 1 iii). The rotation to a magnetocrystalline hard-aligned vortex was occasionally preceded by a rotation to a magnetocrystalline intermediate axis, particularly in TM55 and TM60 particles. SV states aligned with the magnetocrystalline hard axis were found by Nagy et al. (2017) to have extremely low stability, which may be of interest for paleomagnetists. Oblate particles behaved similarly for both ME-SE and MH-SE aniostropies, nucleating a vortex along the short (shape hard) axis of the particle (Figure 3e - f).

Different states were observed in prolate particles depending on elongation direction: In ME-SE particles, a vortex state aligned along the major axis continued to exist without changing up to the maximum size of 500 nm (Figure 3a ii) and continued un-

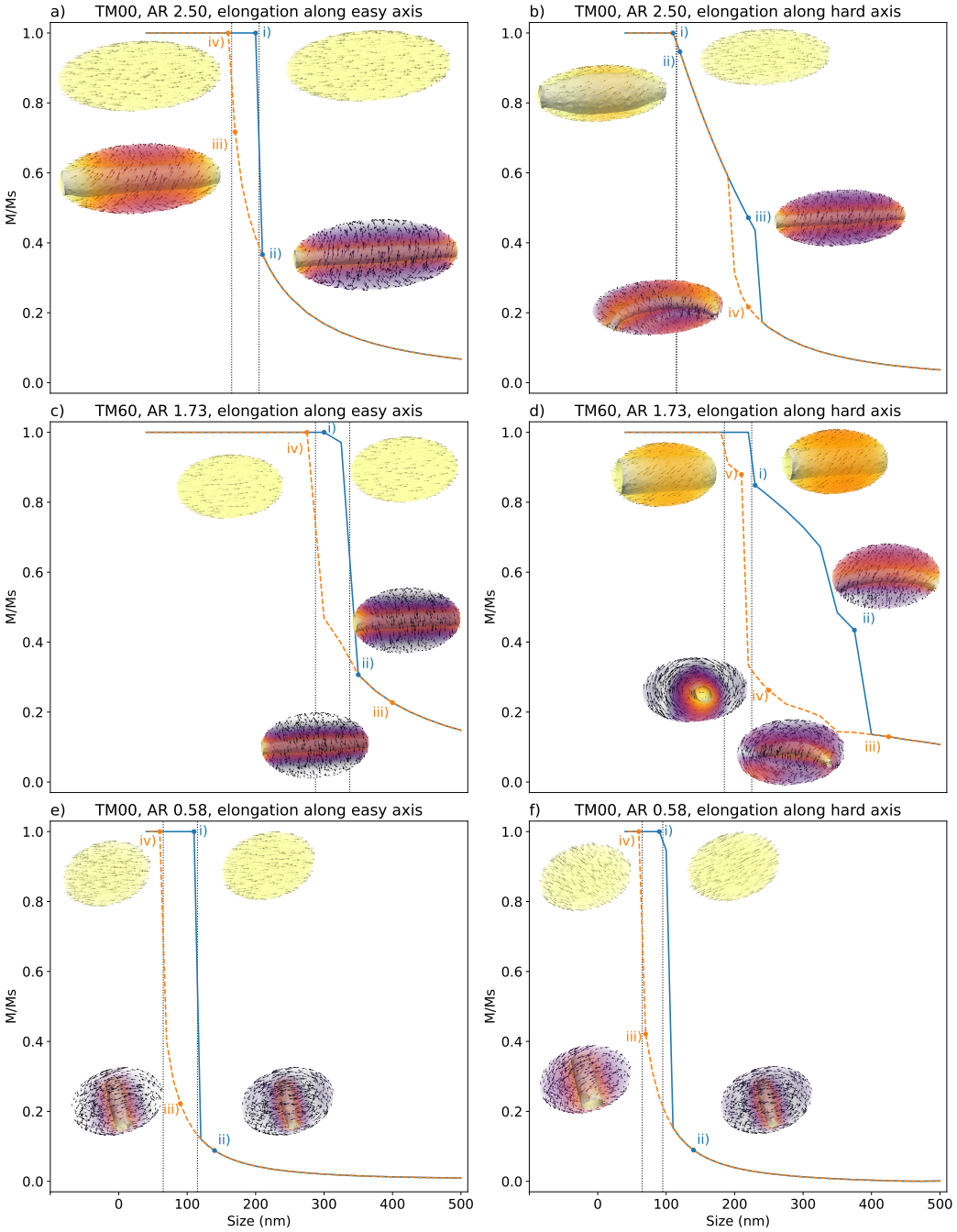

Figure 3. Example size hysteresis loop for particles elongated along the magnetocrystalline easy axis (left column) and for the same particles elongated along the magnetocrystalline hard axis (right column). a - b) size hysteresis loop for a prolate magnetite particle with an axial ratio of 2.50. c - d) size hysteresis loop for a prolate TM60 particle with an axial ratio of 1.73. e - f) size hysteresis loop for an oblate particle with an axial ratio of 0.58. In all plots, the numerals i), ii), iii), iv), v) denote the order in which the minimizations were performed, and the colours represent the growing (blue) or shrinking (orange) branch. $d_{\min}$ and $d_{\max}$ are plotted as vertical dotted lines.

changed down to $d_{\min}$ (Figure 3a iii). By contrast, in MH-SE particles, a secondary sharp drop in the magnetization was observed at sizes above $d_{\max}$, with the SV state along the major axis (Figure 3b iii) transitioning to a state with a curved vortex core which had its ends deflected away from the major axis (Figure 3b iv). These cores were deflected in a variety of directions, forming "Banana" or "S" shapes depending on the whether the two ends of the core were deflected in adjacent or opposing directions. The deflected vortex structures persisted to lower sizes on the shrinking branch than on the growing branch, leading to another "loop" on the size hysteresis diagrams. The transition at $d_{\min}$ for MH-SE particles was often more subtle than for ME-SE ones, with little change in energy, and often a closed loop ($d_{\min} = d_{\max}$) e.g. Fig 3b).

The "S" shaped vortices were frequently observed undergoing rotations during the shrinking branch of the size hysteresis loop, with the core rotating to lie along one of the short (shape-hard) axes of the particle, similar to the states observed in Nagy et al. (2022), which were found to cause pTRM tails in paleointensity experiments. This behaviour can be seen in Figure 3d ii-iv, and occurred most frequently in prolate particles with axial ratios between 1 and 2. This rotation to a short axis was occasionally observed in ME-SE particles, but was far less prevalent overall.

3.3 Trends in $d_{\min}$ and $d_{\max}$

The critical domain transition sizes for $d_{\min}$ and $d_{\max}$ for each composition and shape are presented as contour plots and surfaces in Figure 4. To obtain $d_{\min}$ and $d_{\max}$ as a continuous function of TM composition and axial ratio, the extant data were interpolated using a piecewise cubic 2D interpolation routine. White dashed contours with 100 nm spacing are used to highlight regions where $d_{\max}$ was greater than 500 nm, where a rapid increase occurs. Additionally, some regions of the $d_{\min}$ and $d_{\max}$ surfaces are missing from this dataset. This is because the SD state persists beyond 1 μm during the growing branch of the size hysteresis loop. Obtaining $d_{\min}$ and $d_{\max}$ for loops above this size becomes rapidly more computationally expensive

The surfaces displayed in Figure 4 exhibit some consistent trends with both size and shape. Slices through these surfaces (represented by thick lines on Figure 4a, b and d) at constant composition or axial ratio are displayed in Figure 5. The most noticeable feature of the surfaces is that $d_{\max}$ sharply increases for both prolate and oblate particles relative to equidimensional ones for all compositions (Figure 4a,c). By contrast $d_{\min}$ tends to increase with increasing axial ratio across almost all shapes. The relationship between $d_{\max}$ and TM composition is more complicated. For equidimensional particles, $d_{\max}$ appears to increase rapidly for compositions from TM00 - TM40, decrease from TM40 - TM50, followed by another increase to TM55 and a decrease to TM60. This broad trend is observed for all other shapes where data are available. $d_{\min}$ tends to increase relatively uniformly with increasing TM composition.

The $d_{\min}$ and $d_{\max}$ surfaces for both the ME-SE and MH-SE particles are displayed in Figure 6. It is apparent that the $d_{\max}$ surface in Figure 4 is similar to the ME-SE surface, except at the highest TM compositions. This is primarily driven by the reduced $d_{\max}$ for prolate MH-SE particles, with many of the loops being closed (i.e, $d_{\min} = d_{\max}$). The anisotropy for MH-SE particles has a less uniaxial character, and so the SD structure cannot be a LEM state at larger sizes. The LEM states in the ME-SE particles change rapidly from an SD structure to a vortex structure, accompanied by a sharp drop in the net magnetization (Figure 3a i to ii) By contrast, the MH-SE particles change more gradually from an SD to an SV structure (Figure 3b i to ii), with the first SV states having wide vortex cores encompassing nearly the entire particle. There is also a reduction in $d_{\max}$ for MH-SE oblate surfaces (Figure 3e - f), particularly at intermediate TM compositions.

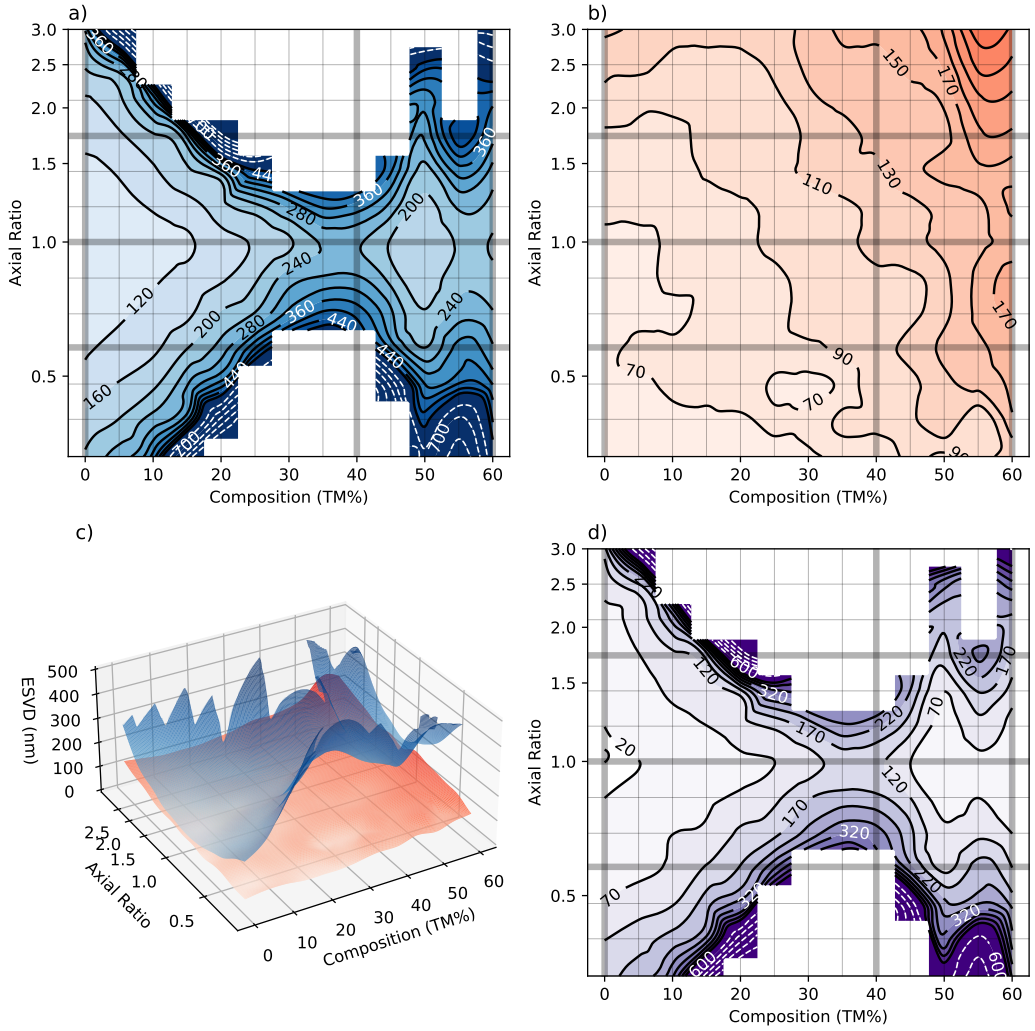

Figure 4. Plots of the maximum $d_{\max}$ and minimum $d_{\min}$ of the ME-SE and MH-SE anisotropies as a function of composition and shape. a) Contour plot of the maximum size at which the SD structure was observed on growing ($d_{\max}$). b) Contour plot of the minimum size at which the SV structure was observed when shrinking ($d_{\min}$). c) 3D surface plot of the $d_{\min}$ and $d_{\max}$ surfaces in a and b. d) Contour plot of the difference (in nm) between the surfaces shown in a, b and c. This represents the range of sizes where both the SD and SV structures are available to a particle of this composition and geometry. The surface and contour plots shown here are produced from a smoothed cubic spline surface fit to the data, with the original data located on the corners of the grid. Thicker grid lines show the locations of slices through the contour plot shown in Figure 5. White dashed contours represent wider spacings of 100 nm in regions where $500 < d_{\max} < 1000$ nm, where the models may be less precise. Note that for ease of viewing, the surface in c is truncated at 500 nm. $d_{\max}$ data are missing for particles that remained in the SD structure after growing to 1 μm.

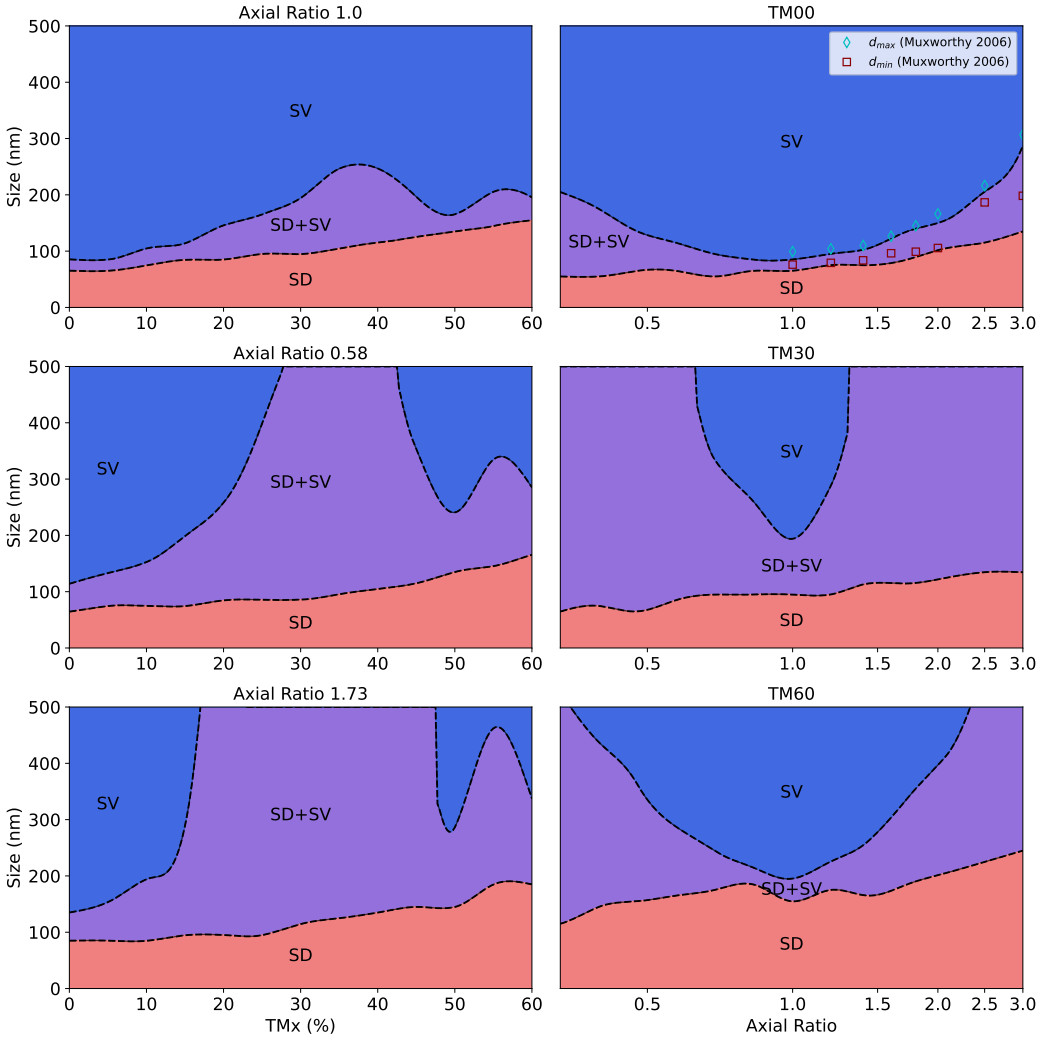

Figure 5. Slices through surfaces displayed in Figure 4. Blue represents regions above the upper surface where the SV structure (and other more complicated states) is available. Red represents the region in which the SD structure is available. Purple represents the range of sizes in which the SD and SV structures are both available. For the TM00 (magnetite) composition, the minimum $d_{\min}$ and maximum $d_{\max}$ of Muxworthy and Williams (2006) are plotted as red squares and blue diamonds for comparison.

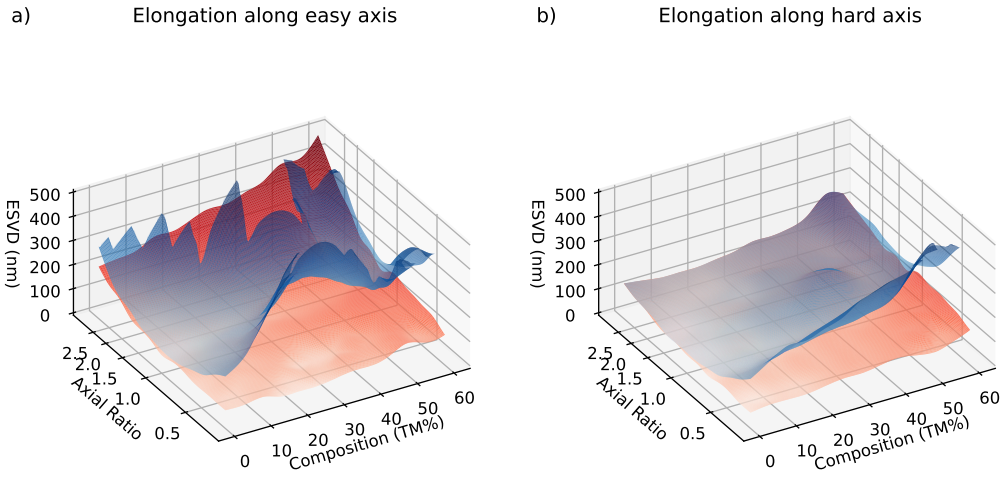

Figure 6. Critical size surfaces for ME-SE (left) vs MH-SE (right) particles. The presentation of these surfaces is the same as in Figure 4c.

4 Discussion

4.1 Comparison to other studies

Our results provide the first description of the domain states present in titanomagnetites using modern micromagnetic models. Our maps of the size ranges of the SD and SV structures follow the work of Butler and Banerjee (1975), but our results are based on unconstrained, inhomogeneous 3-D models. This allows us to evaluate the true LEM states not available from classic Kittel two-domain structure calculations. Additionally, our titanomagnetite material parameters are empirically derived using far more data than were available to Butler and Banerjee, and include the second magnetocrystalline anisotropy constant k_2. This robust physical basis, combined with the increased scale and resolution of our models, enables us to make realistic predictions about the domain states of remanence carriers in igneous rocks. This in turn enables us to identify carriers with potential to cause problematic behaviors in paleomagnetic experiments.

The results presented in Section 3 are most quantitatively comparable to those of Muxworthy and Williams (2006), who applied the size-hysteresis algorithm for prolate magnetite parallelipipeds. We extend this approach to 12 additional compositions and oblate geometries. Our results for $d_{\min}$ and $d_{\max}$ in magnetite are compared to theirs (converted to ESVD) in Figure 5. The $d_{\max}$ data follow a very similar trend with our $d_{\max}$ values being slightly smaller for all elongations. The $d_{\min}$ values are also mostly consistent, but Muxworthy & Williams observe a large increase in $d_{\min}$ at an axial ratio of 2.5, which is not seen in our data. The general similarity between the trends in both studies is encouraging, demonstrating the reproducibility of the size-hysteresis algorithm.

The discrepancy between some of our $d_{\min}$ values and those of Muxworthy and Williams (2006) can be explained by numerous differences between our methodology and theirs; The material parameters for magnetite used are slightly different, our domain states are defined differently, Muxworthy & Williams used a micromagnetic method involving a fast fourier transform rather than the finite element method currently used in MERRILL, and our results are for ellipsoidal particles rather than parallelepipeds. Ellipsoids were

used because faceted surfaces affect the available domain states available to a particle, an effect known as configurational anisotropy (see W. Williams et al., 2006 for a detailed discussion). The ellipsoidal geometry minimizes the effect of configurational anisotropy by minimizing the size of faceted surfaces, ensuring that the dominant controls on $d_{\min}$ and $d_{\max}$ are composition and axial ratio.

Usov and Serebryakova (2023) calculated the energies of different domain states present in magnetite ellipsoids, using a different algorithm to that employed in MERRILL. They calculated a critical size, defined as the size at which the energy of the SV structure was lower than that of the SD structure. These critical sizes lie between our $d_{\min}$ and $d_{\max}$ when converted to ESVD, which should be expected as our critical sizes are bounds on the existence of the structures. The authors findings also shared three common features with ours; Firstly, differences between the size ranges of domain structures in ME-SE and MH-SE particles. Secondly, SD and SV structures existing in overlapping size ranges. Finally, SV states aligned with a variety of magnetocrystalline and shape easy/hard directions. These similarities when using a different software, algorithm, and material parameters suggest that these features are robust properties of titanomagnetites.

4.2 Domain states and instability

The range of sizes between $d_{\min}$ and $d_{\max}$, where both the SD and SV structures can exist, is largest for highly elongated or flattened particles and intermediate TM compositions. Within this range of sizes, the magnetocrystalline hard-aligned vortex observed by Nagy et al. (2017) is observed in equidimensional particles, and the multiple available domain states could lead to non-ideal "pTRM tail" type behaviour in paleointensity experiments. The "unstable zone" of Nagy et al. containing magnetocrystalline hard-aligned vortices was only found to be ~ 10 nm wide for equidimensional magnetite, but we demonstrate that for other compositions and geometries, there are multiple available domain states that can exist over many hundreds of nanometers.

A second region with multiple domain structures was observed in prolate MH-SE particles at larger sizes than $d_{\max}$ (e.g. Figure 3b, d). In this region, an SV state aligned with the long (shape-easy) of the particle coexists with a state where the ends of the vortex core are deflected away from this axis. The deflection is likely related to the influence of the magnetocrystalline easy axes, which could pull the core away from the shape-easy direction towards one of a number of magnetocrystalline-easy directions. Upon further shrinking, the vortex core rotated further and shape-hard aligned SV states were frequently observed. The multiplicity of states offered by the different magnetocrystalline and shape directions, and the wide range of sizes over which these states overlap with the SV state suggest that there may be a second "unstable zone" in prolate MH-SE particles above $d_{\max}$ and into the SV size range. Nagy et al. (2022) simulated pTRM tail behaviour using a prolate faceted magnetite particle that did not have any single-domain LEM states, supporting this hypothesis.

Without thermal energy barriers, size hysteresis experiments cannot calculate the stability of individual particles, but the $d_{\min}$ and $d_{\max}$ sizes represent bounds on a region of interest, which should be a target for future micromagnetic studies. Energy barrier calculations for particles in this region may further our understanding of the pTRM tail phenomenon. Equidimensional particles near $d_{\min}$ and prolate MH-SE particles should be of particular interest to researchers studying this phenomenon, as they exhibit the largest variety of states including the magnetocrystalline hard-aligned vortices of Nagy et al. (2017) and the shape hard-aligned vortices of Nagy et al. (2022).

4.3 The effect of elongation direction

Overall, our findings indicate that the domain states available to magnetic particles have a dependence on the alignment of the magnetocrystalline and shape easy axes (as seen in Figures 3 and 6). This effect has also been observed in micromagnetic algorithms using magnetite cuboids by Muxworthy and Williams (2006) and recently in magnetite ellipsoids by Usov and Serebryakova (2023). Our results indicate that this effect may be even more important than previously thought, as we observe domain states in prolate titanomagnetites that are only present when the elongation direction is along a shape hard axis, which may cause instability as multiple domain states exist in this region.

There have been few observations of the relationship between the elongation direction and magnetization direction in natural samples. Feinberg et al. (2004) used the Electron Back-Scatter Diffraction (EBSD) technique to make observations about the orientations of prolate magnetite particles exsolved in clinopyroxene, and Ageeva et al. (2020) used the same technique to investigate particles exsolved in plagioclase. Both found magnetite particles elongated along the <1 1 1> (magnetocrystalline easy) and <1 1 0> (intermediate) directions. By contrast, Li et al. (2020) recently found that bullet shaped magnetite particles in chains of magnetosomes were predominantly elongated along the <1 0 0> (hard) axis. These limited studies indicate that there is varying competition between shape and magnetocrystalline axes in natural samples, with the dominant anisotropies being strongly tied to the mechanism of particle growth. More EBSD observations of the elongation directions in titanomagnetites of different origins will be necessary to constrain the available domain states in a wider range of real samples.

5 Conclusions

We present a comprehensive set of results from micromagnetic models to determine the range of possible domain states in ellipsoidal titanomagnetite particles of varying size, shape and composition. Previous micromagnetic models characterizing the domain states in samples have focused solely on equidimensional and prolate magnetite particles. The range of compositions and shapes described in our study increase the number of existing domain state characterizations by more than an order of magnitude, improving our understanding of a much wider range of remanence carriers.

For each titanomagntite composition and geometry, we find the critical size at which a single domain (SD) magnetization transitions to a single vortex (SV) magnetization upon growing a particle ($d_{\max}$) and the size at which an SV magnetization transitions to an SD magnetization on shrinking the particle ($d_{\min}$). Particles between these sizes can be magnetized both in the single domain structure, and the single vortex structure. This is significant, as for these particles we observe vortex structures aligned along the magnetocrystalline hard axis, which were found to be unstable by Nagy et al. (2017). Our results indicate that titanomagnetite particles of intermediate composition have a larger range of sizes where both the SD and SV structures are available, and that this range of sizes is larger for both oblate and prolate particles than for equidimensional ones.

Further, we find that the angle between the magnetocrystalline and shape easy axes has a significant effect on the observed domain states in a particle. Prolate particles have a much larger SD + SV size range when their elongation direction is along the magnetocrystalline easy axis (ME-SE) than when along the hard axis (MH-SE). MH-SE prolate particles exhibit "S" and "Banana" states in the SV size range, where the vortex core of the magnetization is deflected away from the elongation direction. These states sometimes rotate to the particle's short axis on shrinking, leading to a potential second "unstable zone" in titanomagnetites. Further investigation of the relationship between par-

ticle shape and crystallographic directions in natural samples should be undertaken to better understand this effect.

Overall, we show that the domain states available to grains vary as a function of shape and composition. The domain states observed indicate that the range of sizes, shapes and compositions of unstable remanence carriers that cause problematic behavior in paleomagnetic studies could be far larger than previously demonstrated. A prevalence of these carriers could explain the high failure rate of paleointensity experiments seen in paleomagnetic literature. Future work will focus on the unstable particles identified in this study to understand the effects of these instabilities on paleomagnetic experiments.

Open Research

The micromagnetic models were produced using the open source micromagnetic modeling MERRILL (Ó Conbhuí et al., 2018; W. Williams et al., n.d.), which is available under a CC-BY-SA 4.0 International license at `https://bitbucket.org/wynwilliams/merrill/`. A Zenodo repository containing a spreadsheet of results, as well as example scripts to reproduce this research can be found at `https://doi.org/10.5281/zenodo.10471806` (Cych, 2024).

Acknowledgements

B.C. and G.A.P. acknowledge funding from Natural Environmental Research Council (NERC) grant NE/W006707/1. G.A.P. further acknowledges a NERC Independent Research Fellowship (NE/P017266/1). L.N. acknowledges funding from NERC Independent Research Fellowship NE/V014722/1. W.W. acknowledges NERC grants NE/S001018/1 and NE/V001388/1. The Institute for Rock Magnetism (IRM) is a US National Multiuser Facility supported through the Instrumentation and Facilities program of the National Science Foundation, Earth Sciences Division, award NSF-EAR 2153786, and by funding from the University of Minnesota. This is IRM publication number 2401.

References

Ageeva, O., Bian, G., Habler, G., Pertsev, A., & Abart, R. (2020). Crystallographic and shape orientations of magnetite micro-inclusions in plagioclase. *Contrib. Mineral. Petrol.*, *175*(10), 1–16. doi: 10.1007/s00410-020-01735-8

Ahn, H.-S., Kidane, T., Yamamoto, Y., & Otofuji, Y.-i. (2016). Low geomagnetic field intensity in the matuyama chron: palaeomagnetic study of a lava sequence from afar depression, east africa. *Geophysical Journal International*, *204*(1), 127–146.

Akimoto, S.-i., Katsura, T., & Yoshida, M. (1957). Magnetic properties of $TiFe_2O_4$-Fe_3O_4 system and their change with oxidation. *J. Geomagn. Geoelec.*, *9*(4), 165–178. doi: 10.5636/jgg.9.165

Aragón, R. (1992). Cubic magnetic anisotropy of nonstoichiometric magnetite. *Physical Review B*, *46*(9), 5334.

Ayachit, U. (2015). *The paraview guide: a parallel visualization application*. Kitware, Inc.

Banerjee, S. K. (1991). Magnetic properties of Fe-Ti oxides. In D. H. Lindsley (Ed.), *Oxide minerals: Petrologic and magnetic significance* (pp. 107–128). Berlin, Boston: De Gruyter. doi: 10.1515/9781501508684-007

Bickford, L., Brownlow, J., & Penoyer, R. (1957). Magnetocrystalline anisotropy in cobalt-substituted magnetite single crystals. *Proceedings of the IEE-Part B: Radio and Electronic Engineering*, *104*(5S), 238–244.

Bickford Jr, L. (1950). Ferromagnetic resonance absorption in magnetite single crystals. *Physical Review*, *78*(4), 449.

Bleil, U. (1976). An experimental study of the titanomagnetite solid solution series. *Pure and Applied geophysics*, *114*, 165–175.

Böhnel, H. N., Dekkers, M. J., Delgado-Argote, L. A., & Gratton, M. N. (2009). Comparison between the microwave and multispecimen parallel difference ptrm paleointensity methods. *Geophysical Journal International*, *177*(2), 383–394.

Bol'Shakov, A. (1979). A thermomagnetic criterion for determining the domain structure of ferrimagnetics. *Izv. Acad. Sci. USSR Phys. Solid Earth*, *15*, 111–117.

Bowles, J. A., Gerzich, D. M., & Jackson, M. J. (2018). Assessing new and old methods in paleomagnetic paleothermometry: a test case at Mt. St. Helens, USA. *Geochemistry, Geophysics, Geosystems*, *19*(6), 1714–1730.

Bowles, J. A., Morris, A., Tivey, M., & Lascu, I. (2020). Magnetic mineral populations in lower oceanic crustal gabbros (Atlantis bank, SW Indian ridge): Implications for marine magnetic anomalies. *Geochemistry, Geophysics, Geosystems*, *21*(3), e2019GC008847.

Brown, W. F. B. (1963). *Micromagnetics.* New York: John Wiley & Sons.

Butler, R. F., & Banerjee, S. K. (1975). Theoretical single-domain grain size range in magnetite and titanomagnetite. *J. Geophys. Res.*, *80*(29), 4049–4058. doi: 10.1029/JB080i029p04049

Calhoun, B. (1954). Magnetic and electric properties of magnetite at low temperatures. *Physical Review*, *94*(6), 1577.

Calvo, M., Prévot, M., Perrin, M., & Riisager, J. (2002). Investigating the reasons for the failure of palaeointensity experiments: a study on historical lava flows from Mt. Etna (Italy). *Geophysical journal international*, *149*(1), 44–63.

Calvo-Rathert, M., Bógalo, M. F., Gogichaishvili, A., Sologashvili, J., & Vashakidze, G. (2013). New paleomagnetic and paleointensity data from pliocene lava flows from the lesser caucasus. *Journal of Asian Earth Sciences*, *73*, 347–361.

Calvo-Rathert, M., Goguitchaichvili, A., Bógalo, M.-F., Vegas-Tubía, N., Carrancho, Á., & Sologashvili, J. (2011). A paleomagnetic and paleointensity study on pleistocene and pliocene basaltic flows from the djavakheti highland (southern georgia, caucasus). *Physics of the Earth and Planetary interiors*, *187*(3-4), 212–224.

Calvo-Rathert, M., Goguitchaichvili, A., & Vegas-Tubia, N. (2009). A paleointensity study on middle miocene to pliocene volcanic rocks from south-eastern spain. *Earth, planets and space*, *61*, 61–69.

Carvallo, C., Camps, P., Ruffet, G., Henry, B., & Poidras, T. (2003). Mono lake or Laschamp geomagnetic event recorded from lava flows in Amsterdam island (southeastern Indian Ocean). *Geophysical Journal International*, *154*(3), 767–782.

Carvallo, C., Özdemir, Ö., & Dunlop, D. J. (2004). Palaeointensity determinations, palaeodirections and magnetic properties of basalts from the Emperor seamounts. *Geophysical Journal International*, *156*(1), 29–38.

Chauvin, A., Gillot, P.-Y., & Bonhommet, N. (1991). Paleointensity of the Earth's magnetic field recorded by two late quaternary volcanic sequences at the island of La Réunion (Indian ocean). *Journal of Geophysical Research: Solid Earth*, *96*(B2), 1981–2006.

Chikazumi, S. (1964). *Physics of magnetism.* John Wiley & Sons.

Coe, R. S., Grommé, S., & Mankinen, E. A. (1978). Geomagnetic paleointensities from radiocarbon-dated lava flows on Hawaii and the question of the pacific nondipole low. *Journal of Geophysical Research: Solid Earth*, *83*(B4), 1740–1756.

Coe, R. S., Gromme, S., & Mankinen, E. A. (1984). Geomagnetic paleointensities from excursion sequences in lavas on Oahu, Hawaii. *Journal of Geophysical Research: Solid Earth*, *89*(B2), 1059–1069.

Coreform LLC. (2017). *Coreform Cubit, v2022.4 (64-Bit).* Retrieved from `https://`

516 coreform.com

517 Cych, B. (2024). *Titanomagnetite size hysteresis.* Zenodo. Retrieved from
518 https://doi.org/10.5281/zenodo.10471806 (Software) doi: 10.5281/
519 zenodo.10471806

520 de Groot, L. V., Dekkers, M. J., & Mullender, T. A. (2012). Exploring the potential
521 of acquisition curves of the anhysteretic remanent magnetization as a tool to
522 detect subtle magnetic alteration induced by heating. *Physics of the Earth and*
523 *Planetary Interiors*, *194*, 71–84.

524 de Groot, L. V., Mullender, T. A., & Dekkers, M. J. (2013). An evaluation of the
525 influence of the experimental cooling rate along with other thermomagnetic
526 effects to explain anomalously low palaeointensities obtained for historic lavas
527 of Mt Etna (Italy). *Geophysical Journal International*, *193*(3), 1198–1215.

528 Donadini, F., Elming, S.-Å., Tauxe, L., & Hålenius, U. (2011). Paleointensity de-
529 termination on a 1.786 ga old gabbro from Hoting, central Sweden. *Earth and*
530 *Planetary Science Letters*, *309*(3-4), 234–248.

531 Dunlop, D. J., & Özdemir, Ö. (2001). Beyond Néel's theories: thermal demagne-
532 tization of narrow-band partial thermoremanent magnetizations. *Phys. Earth*
533 *Planet. Inter.*, *126*(1), 43–57. doi: 10.1016/S0031-9201(01)00243-6

534 Dunlop, D. J., & Özdemir, Ö. (1997). *Rock magnetism: fundamentals and frontiers*
535 (No. 3). Cambridge university press.

536 Fabian, K., Kirchner, A., Williams, W., Heider, F., Leibl, T., & Huber, A. (1996).
537 Three-dimensional micromagnetic calculations for magnetite using FFT. *Geo-*
538 *phys. J. Int.*, *124*(1), 89–104. doi: 10.1111/j.1365-246X.1996.tb06354.x

539 Feinberg, J. M., Harrison, R. J., Kasama, T., Dunin-Borkowski, R. E., Scott, G. R.,
540 & Renne, P. R. (2006). Effects of internal mineral structures on the magnetic
541 remanence of silicate-hosted titanomagnetite inclusions: An electron hologra-
542 phy study. *Journal of Geophysical Research: Solid Earth*, *111*(B12).

543 Feinberg, J. M., Wenk, H.-R., Renne, P. R., & Scott, G. R. (2004). Epitaxial
544 relationships of clinopyroxene-hosted magnetite determined using electron
545 backscatter diffraction (EBSD) technique. *Am. Mineral.*, *89*(2-3), 462–466.
546 doi: 10.2138/am-2004-2-328

547 Ferk, A., Aulock, F. v., Leonhardt, R., Hess, K.-U., & Dingwell, D. (2010). A
548 cooling rate bias in paleointensity determination from volcanic glass: An ex-
549 perimental demonstration. *Journal of Geophysical Research: Solid Earth*,
550 *115*(B8).

551 Ferk, A., Denton, J., Leonhardt, R., Tuffen, H., Koch, S., Hess, K.-U., & Dingwell,
552 D. (2012). Paleointensity on volcanic glass of varying hydration states. *Physics*
553 *of the Earth and Planetary Interiors*, *208*, 25–37.

554 Fletcher, E., & O'Reilly, W. (1974). Contribution of Fe^{2+} ions to the magnetocrys-
555 talline anisotropy constant k_1 of $Fe_{3-x}Ti_xO_4$ ($0 < x < 1$). *Journal of Physics*
556 *C: Solid State Physics*, *7*(1), 171.

557 Fontana, G., Mac Niocaill, C., Brown, R. J., Sparks, R. S. J., & Field, M. (2011).
558 Emplacement temperatures of pyroclastic and volcaniclastic deposits in kim-
559 berlite pipes in southern Africa. *Bulletin of Volcanology*, *73*, 1063–1083.

560 Fredkin, D., & Koehler, T. (1987). Numerical micromagnetics by the finite element
561 method. *IEEE Transactions on Magnetics*, *23*(5), 3385–3387.

562 Gonzalez, S., Sherwood, G., Böhnel, H., & Schnepp, E. (1997). Palaeosecular vari-
563 ation in central mexico over the last 30000 years: the record from lavas. *Geo-*
564 *physical Journal International*, *130*(1), 201–219.

565 Hauptman, Z. (1974). High temperature oxidation, range of non-stoichiometry and
566 curie point variation of cation deficient titanomagnetite $Fe_{2.4}Ti_{0.6}O_{4+\gamma}$. *Geo-*
567 *physical Journal International*, *38*(1), 29–47.

568 Heider, F., & Williams, W. (1988). Note on temperature dependence of exchange
569 constant in magnetite. *Geophysical Research Letters*, *15*(2), 184–187.

570 Hill, M. J., & Shaw, J. (1999). Palaeointensity results for historic lavas from Mt

Etna using microwave demagnetization/remagnetization in a modified Thellier-type experiment. *Geophysical Journal International*, *139*(2), 583–590.

Hill, M. J., & Shaw, J. (2000). Magnetic field intensity study of the 1960 Kilauea lava flow, Hawaii, using the microwave palaeointensity technique. *Geophysical Journal International*, *142*(2), 487–504.

Hunt, C. P., Moskowitz, B. M., & Banerjee, S. K. (1995). Magnetic properties of rocks and minerals. *Rock physics and phase relations: A handbook of physical constants*, *3*, 189–204.

Kąkol, Z., Sabol, J., & Honig, J. (1991a). Cation distribution and magnetic properties of titanomagnetites $Fe_{3-x}Ti_xO_4$ ($0 \leq x < 1$). *Physical Review B*, *43*(1), 649.

Kąkol, Z., Sabol, J., & Honig, J. (1991b). Magnetic anisotropy of titanomagnetites $Fe_{3-x}Ti_xO_4$ ($0 \leq x < 0.55$). *Physical Review B*, *44*(5), 2198.

Kąkol, Z., Sabol, J., Stickler, J., Kozłowski, A., & Honig, J. (1994). Influence of titanium doping on the magnetocrystalline anisotropy of magnetite. *Physical Review B*, *49*(18), 12767.

Keefer, C. M., & Shive, P. N. (1981). Curie temperature and lattice constant reference contours for synthetic titanomaghemites. *Journal of Geophysical Research: Solid Earth*, *86*(B2), 987–998.

Khakhalova, E., Moskowitz, B. M., Williams, W., Biedermann, A. R., & Solheid, P. (2018). Magnetic vortex states in small octahedral particles of intermediate titanomagnetite. *Geochem. Geophys. Geosyst.*, *19*(9), 3071–3083. doi: 10.1029/2018GC007723

Kittel, C. (1949). Physical theory of ferromagnetic domains. *Reviews of modern Physics*, *21*(4), 541.

Kono, M. (1974). Intensities of the Earth's magnetic field about 60 my ago determined from the Deccan trap basalts, India. *Journal of Geophysical Research*, *79*(8), 1135–1141.

Kono, M., & Tosha, T. (1980). Geomagnetic paleointensity measurements on leg 55 basalts. *Init. Repts. DSDP*, 753–758.

Larson, E., Ozima, M., Ozima, M., Nagata, T., & Strangway, D. (1969). Stability of remanent magnetization of igneous rocks. *Geophysical Journal International*, *17*(3), 263–292.

Li, J., Menguy, N., Roberts, A. P., Gu, L., Leroy, E., Bourgon, J., ... Pan, Y. (2020). Bullet-shaped magnetite biomineralization within a magnetotactic deltaproteobacterium: Implications for magnetofossil identification. *J. Geophys. Res. Biogeosci.*, *125*(7), e2020JG005680. doi: 10.1029/2020JG005680

Mankinen, E. A. (1994). *Preliminary geomagnetic paleointensities from long valley caldera, california*. US Geological Survey.

Martín-Hernández, F., Bominaar-Silkens, I. M., Dekkers, M. J., & Maan, J. K. (2006). High-field cantilever magnetometry as a tool for the determination of the magnetocrystalline anisotropy of single crystals. *Tectonophysics*, *418*(1-2), 21–30.

Matzka, J., & Krása, D. (2007). Oceanic basalt continuous thermal demagnetization curves. *Geophysical Journal International*, *169*(3), 941–950.

Michalk, D. M., Biggin, A. J., Knudsen, M. F., Böhnel, H. N., Nowaczyk, N. R., Ownby, S., & López-Martínez, M. (2010). Application of the multispecimen palaeointensity method to pleistocene lava flows from the Trans-Mexican volcanic belt. *Physics of the Earth and Planetary Interiors*, *179*(3-4), 139–156.

Moskowitz, B. M. (1980). Theoretical grain size limits for single-domain, pseudo-single-domain and multi-domain behavior in titanomagnetite (x = 0.6) as a function of low-temperature oxidation. *Earth Planet. Sci. Lett.*, *47*(2), 285–293. doi: 10.1016/0012-821X(80)90045-X

Moskowitz, B. M. (1993). High-temperature magnetostriction of magnetite and titanomagnetites. *Journal of Geophysical Research: Solid Earth*, *98*(B1), 359–

371.

Moskowitz, B. M., & Halgedahl, S. L. (1987). Theoretical temperature and grain-size dependence of domain state in x= 0.6 titanomagnetite. *Journal of Geophysical Research: Solid Earth*, *92*(B10), 10667–10682.

Moskowitz, B. M., Jackson, M., & Kissel, C. (1998). Low-temperature magnetic behavior of titanomagnetites. *Earth and Planetary Science Letters*, *157*(3-4), 141–149.

Muxworthy, A. R., & Williams, W. (2006). Critical single-domain/multidomain grain sizes in noninteracting and interacting elongated magnetite particles: Implications for magnetosomes. *J. Geophys. Res. Solid Earth*, *111*(B12). doi: 10.1029/2006JB004588

Muxworthy, A. R., & Williams, W. (2015). Critical single-domain grain sizes in elongated iron particles: implications for meteoritic and lunar magnetism. *Geophys. J. Int.*, *202*(1), 578–583. doi: 10.1093/gji/ggv180

Muxworthy, A. R., Williams, W., Roberts, A. P., Winklhofer, M., Chang, L., & Pósfai, M. (2013). Critical single domain grain sizes in chains of interacting greigite particles: Implications for magnetosome crystals. *Geochem. Geophys. Geosyst.*, *14*(12), 5430–5441. doi: 10.1002/2013GC004973

Nagy, L., Williams, W., Muxworthy, A. R., Fabian, K., Almeida, T. P., Conbhuí, P. Ó., & Shcherbakov, V. P. (2017). Stability of equidimensional pseudo–single-domain magnetite over billion-year timescales. *Proc. Natl. Acad. Sci. U.S.A.*, *114*(39), 10356–10360. doi: 10.1073/pnas.1708344114

Nagy, L., Williams, W., Tauxe, L., & Muxworthy, A. (2022). Chasing tails: Insights from micromagnetic modeling for thermomagnetic recording in non-uniform magnetic structures. *Geophys. Res. Lett.*, *49*(23), e2022GL101032. doi: 10.1029/2022GL101032

Nagy, L., Williams, W., Tauxe, L., & Muxworthy, A. R. (2019). From nano to micro: Evolution of magnetic domain structures in multidomain magnetite. *Geochem. Geophys. Geosyst.*, *20*(6), 2907–2918. doi: 10.1029/2019GC008319

Néel, L. (1949). Théorie du traînage magnétique des ferromagnétiques en grains fins avec application aux terres cuites. *Annales de géophysique*, *5*, 99–136.

Newell, A. J., Dunlop, D. J., & Enkin, R. J. (1990). Temperature dependence of critical sizes, wall widths and moments in two-domain magnetite grains. *Physics of the earth and planetary interiors*, *65*(1-2), 165–176.

Nishitani, T., & Kono, M. (1983). Curie temperature and lattice constant of oxidized titanomagnetite. *Geophysical Journal International*, *74*(2), 585–600.

Ó Conbhuí, P. Ó., Williams, W., Fabian, K., Ridley, P., Nagy, L., & Muxworthy, A. R. (2018). MERRILL: Micromagnetic Earth Related Robust Interpreted Language Laboratory. *Geochem. Geophys. Geosyst.*, *19*(4), 1080–1106. doi: 10.1002/2017GC007279

O'Donovan, J., & O'Reilly, W. (1977). The preparation, characterization and magnetic properties of synthetic analogues of some carriers of the palaeomagnetic record. *Journal of geomagnetism and geoelectricity*, *29*(4), 331–344.

Özdemir, Ö., & O'Reilly, W. (1978). Magnetic properties of monodomain aluminium-substituted titanomagnetite. *Physics of the Earth and Planetary Interiors*, *16*(3), 190–195.

Ozima, M., & Larson, E. (1970). Low-and high-temperature oxidation of titanomagnetite in relation to irreversible changes in the magnetic properties of submarine basalts. *Journal of Geophysical Research*, *75*(5), 1003–1017.

Ozima, M., Ozima, M., & Kaneoka, I. (1968). Potassium-argon ages and magnetic properties of some dredged submarine basalts and their geophysical implications. *Journal of Geophysical Research*, *73*(2), 711–723.

Ozima, M., & Sakamoto, N. (1971). Magnetic properties of synthesized titanomaghemite. *Journal of Geophysical Research*, *76*(29), 7035–7046.

Pan, Y., Hill, M. J., & Zhu, R. (2005). Paleomagnetic and paleointensity study of

an oligocene–miocene lava sequence from the Hannuoba basalts in northern China. *Physics of the Earth and Planetary Interiors*, *151*(1-2), 21–35.

Paterson, G. A., Roberts, A. P., Mac Niocaill, C., Muxworthy, A. R., Gurioli, L., Viramonté, J. G., ... Weider, S. (2010). Paleomagnetic determination of emplacement temperatures of pyroclastic deposits: an under-utilized tool. *Bulletin of Volcanology*, *72*, 309–330.

Pauthenet, R., & Bochirol, L. (1951). Aimantation spontanée des ferrites. *J. phys. radium*, *12*(3), 249–251.

Piper, J., Koçbulut, F., Gürsoy, H., Tatar, O., Viereck, L., Lepetit, P., ... Akpınar, Z. (2013). Palaeomagnetism of the Cappadocian volcanic succession, central Turkey: Major ignimbrite emplacement during two short (Miocene) episodes and Neogene tectonics of the Anatolian collage. *Journal of Volcanology and Geothermal Research*, *262*, 47–67.

Rahman, A., & Parry, L. (1978). Titanomagnetites prepared at different oxidation conditions: hysteresis properties. *Physics of the Earth and Planetary Interiors*, *16*(3), 232–239.

Rave, W., Fabian, K., & Hubert, A. (1998). Magnetic states of small cubic particles with uniaxial anisotropy. *Journal of Magnetism and Magnetic Materials*, *190*(3), 332-348. doi: Doi10.1016/S0304-8853(98)00328-X

Readman, P., & O'Reilly, W. (1972). Magnetic properties of oxidized (cation-deficient) titanomagnetites (Fe, Ti, $\square$)$_3$ O$_4$. *Journal of geomagnetism and geoelectricity*, *24*(1), 69–90.

Riisager, P., & Riisager, J. (2001). Detecting multidomain magnetic grains in Thellier palaeointensity experiments. *Physics of the Earth and Planetary Interiors*, *125*(1), 111-117. doi: https://doi.org/10.1016/S0031-9201(01)00236-9

Robins, B. W. (1972). *Remanent magnetization in spinel iron-oxides* (Unpublished doctoral dissertation). UNSW Sydney.

Rolph, T. (1997). An investigation of the magnetic variation within two recent lava flows. *Geophysical Journal International*, *130*(1), 125–136.

Sahu, S., & Moskowitz, B. M. (1995). Thermal dependence of magnetocrystalline anisotropy and magnetostriction constants of single crystal $Fe_{2.4}Ti_{0.6}O_4$. *Geophysical research letters*, *22*(4), 449–452.

Santos, C. N., & Tauxe, L. (2019). Investigating the accuracy, precision, and cooling rate dependence of laboratory-acquired thermal remanences during paleointensity experiments. *Geochem. Geophys. Geosyst.*, *20*(1), 383–397. doi: 10.1029/2018GC007946

Schabes, M. E., & Bertram, H. N. (1988). Magnetization processes in ferromagnetic cubes. *Journal of Applied Physics*, *64*(3), 1347–1357.

Selkin, P. A., Gee, J. S., Meurer, W. P., & Hemming, S. R. (2008). Paleointensity record from the 2.7 Ga Stillwater Complex, Montana. *Geochem. Geophys. Geosyst.*, *9*(12). doi: 10.1029/2008GC001950

Sherwood, G., Shaw, J., Baer, G., & Mallik, S. B. (1993). The strength of the geomagnetic field during the cretaceous quiet zone: palaeointensity results from Israeli and Indian lavas. *Journal of geomagnetism and geoelectricity*, *45*(4), 339–360.

Syono, Y. (1965). Magnetocrystalline anisotropy and magnetostriction of Fe_3O_4-Fe_2TiO_4 series-with special application to rocks magnetism. *Jpn. J. Geophys.*, *4*, 71–143.

Syono, Y., & Ishikawa, Y. (1963). Magnetostriction constants of $x\mathrm{Fe_2TiO_4} \cdot (1 - x)\mathrm{Fe_3O_4}$. *Journal of the Physical Society of Japan*, *18*(8), 1231–1232.

Tanaka, H., & Komuro, N. (2009). The Shaw paleointensity method: Can the ARM simulate the TRM alteration? *Physics of the Earth and Planetary Interiors*, *173*(3-4), 269–278.

Thellier, E. (1941). Sur les propriétés de l'aimantation thermorémanente des terres cuites. *CR Acad. Sci. Paris*, *213*, 1019–1022.

Thellier, E., & Thellier, O. (1941). Sur les variations thermiques de l'aimantation thermorémanente des terres cuites. *CR Hebd. Seances Acad. Sci*, *213*, 59–61.

Tsunakawa, H., & Shaw, J. (1994). The Shaw method of palaeointensity determinations and its application to recent volcanic rocks. *Geophysical Journal International*, *118*(3), 781–787.

Usov, N. A., & Serebryakova, O. N. (2023). Non uniform micromagnetic states in spheroidal magnetite nanoparticles. *J. Magn. Magn. Mater.*, *588*, 171345. doi: 10.1016/j.jmmm.2023.171345

Uyeda, S. (1958). Thermo-remanent magnetism as a medium of paleomagnetism, with special reference to reverse thermo-remanent magnetism. *J. Japan Geophys.*, *2*, 1–123.

Valdez-Grijalva, M. A., Nagy, L., Muxworthy, A. R., Williams, W., & Fabian, K. (2018). The magnetic structure and palaeomagnetic recording fidelity of submicron greigite (Fe_3S_4). *Earth and Planetary Science Letters*, *483*, 76–89.

Vérard, C., Leonhardt, R., Winklhofer, M., & Fabian, K. (2012). Variations of magnetic properties in thin lava flow profiles: Implications for the recording of the Laschamp excursion. *Physics of the Earth and Planetary Interiors*, *200*, 10–27.

Villasante-Marcos, V., & Pavón-Carrasco, F. J. (2014). Palaeomagnetic constraints on the age of lomo negro volcanic eruption (el hierro, canary islands). *Geophysical Journal International*, *199*(3), 1497–1514.

Virtanen, P., Gommers, R., Oliphant, T. E., Haberland, M., Reddy, T., Cournapeau, D., ... SciPy 1.0 Contributors (2020). SciPy 1.0: Fundamental algorithms for scientific computing in Python. *Nature Methods*, *17*, 261–272. doi: 10.1038/s41592-019-0686-2

Wanamaker, B., & Moskowitz, B. M. (1994). Effect of nonstoichiometry on the magnetic and electrical properties of synthetic single crystal $Fe_{2.4}Ti_{0.6}O_4$. *Geophysical Research Letters*, *21*(11), 983–986.

Wang, D., & Van der Voo, R. (2004). The hysteresis properties of multidomain magnetite and titanomagnetite/titanomaghemite in mid-ocean ridge basalts. *Earth and Planetary Science Letters*, *220*(1-2), 175–184.

Wechsler, B. A., Lindsley, D. H., & Prewitt, C. T. (1984). Crystal structure and cation distribution in titanomagnetites ($Fe_{3-x}Ti_xO_4$). *American Mineralogist*, *69*(7-8), 754–770.

Williams, H., & Bozorth, R. (1953). Magnetic study of low temperature transformation in magnetite. *Reviews of Modern Physics*, *25*(1), 79.

Williams, W., & Dunlop, D. J. (1989). Three-dimensional micromagnetic modelling of ferromagnetic domain structure. *Nature*, *337*(6208), 634–637.

Williams, W., Fabian, K., P., R., Nagy, L., Paterson, G. A., & Muxworthy, A. R. (n.d.). *Merrill* [software]. Retrieved from `https://bitbucket.org/wynwilliams/merrill`

Williams, W., Muxworthy, A. R., & Paterson, G. A. (2006). Configurational anisotropy in single-domain and pseudosingle-domain grains of magnetite. *Journal of Geophysical Research: Solid Earth*, *111*(B12).

Witt, A., Fabian, K., & Bleil, U. (2005). Three-dimensional micromagnetic calculations for naturally shaped magnetite: Octahedra and magnetosomes. *Earth Planet. Sci. Lett.*, *233*(3), 311–324. doi: 10.1016/j.epsl.2005.01.043